PHYSICAL REVIEW FLUIDS **3**, 074003 (2018)

Stratified flows in axially rotating pipes

S. Lyu and S. M. Taghavi*
Department of Chemical Engineering, Université Laval, Québec, QC, Canada G1V 0A6

(Received 19 December 2017; published 30 July 2018; corrected 11 June 2020)

We study experimentally the effects of a pipe axial rotation on a stratified displacement flow, using two miscible fluids of different density, in a long inclined pipe. Increasing the pipe rotation speed induces transverse mixing and results in a complete removal of the displaced fluid above a critical transition, described by $\mathrm{Rb} \approx 5/2\pi\ \mathrm{Fr}(1-\mathrm{Fr})^{-1}$, relating the Rossby number (Rb) to a modified Froude number (Fr). In addition, we quantify the variation of the leading and trailing displacement front velocities ($\hat{V}_f$, $\hat{V}_t$), as a function of the mean displacement velocity ($\hat{V}_0$), showing that for $\mathrm{Rb}/\mathrm{Fr} \gtrsim 5/2\pi$ we find $\hat{V}_f \approx 1.3\hat{V}_0$ and $\hat{V}_t \approx 0.8\hat{V}_0$. These findings offer insights to greatly improve displacement efficiency using rotational motion.

DOI: 10.1103/PhysRevFluids.3.074003

I. INTRODUCTION

Displacement flows are frequently observed in natural phenomena and industrial systems; to give a few examples, in lung airways [1], oil well cementing [2], coating and coextrusion [3], and cleaning of processing machinery in food processing [4]. The fluids involved can be miscible and they can have different densities. Displacement flows with a laminar imposed flow in inclined pipes are also typical. It is known that the interpenetration of the displacing and displaced fluids is governed by a combination of buoyancy, stratification, the imposed displacement flow rate, and the flow geometry. From a practical point of view, analyzing these displacement flows may come down to addressing a key question: Is the displacing fluid able to completely remove the *in situ* displaced fluid out of the flow geometry? The answer to this question is often negative, for the most part, due to the complex interaction between various forces, resulting in a weak control over the interpenetration of the fluids. The present paper demonstrates that a pipe axial rotation can significantly affect this interpenetration for buoyant miscible displacement flows in inclined pipes, making a complete removal of the displaced fluid possible.

Our work extends from buoyant miscible lock-exchange flows, for which the literature is fairly developed. While no displacement flow rate is imposed, buoyancy is the only driving force in these flows. Seon *et al.* [5–7] studied in detail the effects of buoyancy in lock-exchange flows in a long inclined pipe. Conceptually similar to the Boycott effect, they noted that at high inclinations (from vertical) the light and heavy fluids are completely segregated and, therefore, they strongly interpenetrate. They quantified the interpenetration front velocities versus an inertial velocity scale, $\sqrt{\mathrm{At}\hat{g}\hat{D}}$ [8], or a viscous velocity scale, $\mathrm{At}\hat{g}\hat{D}^2/\hat{\nu}$, with At denoting the Atwood number, $\hat{g}$ the acceleration due to gravity, $\hat{D}$ the pipe diameter, and $\hat{\nu}$ the kinematic viscosity. Later, Taghavi *et al.* [9,10] considered the effects of a flow rate (with mean velocity $\hat{V}_0$) imposed to confined buoyant flows. Through analyzing the motions of the interpenetration fronts, including the *leading* and *trailing* fronts, they defined a criterion for an efficient displacement based on whether the trailing front moves upstream or downstream [11]. They found that, when buoyancy is strong, the trailing front moves

---

[*] Corresponding author: Seyed-Mohammad.Taghavi@gch.ulaval.ca

continuously upstream against the imposed flow direction; thus, the displacing fluid is not able to completely remove the displaced one (in other words, the displaced fluid is nonremovable).

In spite of detailed studies addressing single-fluid flows in axially rotating pipes (e.g., the classical stability analysis of Pedley [12,13] and Mackrodt [14]), or two-fluid Taylor-Couette flows [15] and rotating core-annular flows [16], it is still hard to predict how a pipe rotation affects stratified buoyant flows. For example, Carrasco-Teja and Frigaard [17] demonstrated numerically that an inner cylinder rotation in annular miscible displacements results in the positioning of heavy fluid above light fluid at certain azimuthal positions, a configuration that is prone to buoyancy-driven fingering. However, they found that the instability remains local, with negligible effects on the longer time displacement dynamics.

Here, we present an experimental study of rotating pipe displacements and demonstrate that the imposition of a pipe axial rotation on a buoyant miscible displacement flow strongly influences the flow patterns, the leading and trailing front velocities, and the physical mechanisms by which the displacement occurs. We propound the idea that a flow geometry rotation can be used to control stratified displacement flows, yielding an efficient removal of the displaced fluid by the displacing one.

Despite its fundamental nature, our work can have significant industrial applications, for instance in oil well primary cementing operations, which involve pumping of cement along a circular pipe (casing) to remove (displace) *in situ* drilling mud. Although there exist various types of casing heads and special adaptors that could enable a casing axial rotation at moderate speeds [2], this approach is not widely used to enhance casing displacements, perhaps due to a serious lack of fundamental knowledge about the effects of such rotation. Our research may help develop a crucial understanding that leads to enhancing displacement efficiently using a pipe rotation and eventually eliminate primary cementing operational failures, which have previously contributed to catastrophic consequences (e.g., the Deepwater Horizon drilling rig explosion [18]).

Below, after briefly discussing our experimental range, we will first present our experimental results, showing qualitatively the general effects of a pipe rotation on buoyant flows (in the Boussinesq limit), with a laminar imposed flow, in an inclined pipe. We will then quantify the leading and trailing front velocities versus the flow parameters. We will analyze the corresponding exchange flows to gain a deeper understanding. Finally, using the dimensionless groups that govern the flow, we will provide a complete displacement flow regime map, based on whether the displaced fluid can be removed by the displacing fluid.

II. METHODS AND MATERIALS

A. Experimental setup

Our experiments were performed in a transparent pipe (acrylic) with the length of $\hat{L} = 3$ m and the inner circular diameter of $\hat{D} = 19.05$ mm (see Fig. 1). The pipe was split into two parts (2.3 and 0.7 m) by an automated pneumatic gate valve (VAT, Inc.), to completely separate displacing and displaced fluids before running each experiment. The pipe was mounted on a robust frame, which could be tilted to any inclination angles, between 0° and 90°, measured from vertical (β). An elevated tank filled with the heavier fluid was connected to the pipe and provided stable imposed flow (with mean velocity $\hat{V}_0$) driven by gravity only. A system of a stepper motor and various connectors, controlled by LabView, produced stable pipe rotations around its axis of symmetry, at precise rotation speeds ($\hat{\omega}$), taking $\sim 10^{-3}$ s to reach steady state. Six vertical supports were included in the setup so that any pipe vibrations or fluctuations remained below 10^{-1} mm even at high rotation speeds.

The upper and lower parts of the pipe were filled with displacing and displaced fluids, using procedures that minimized bubble formations, while miniature valves were installed near the gate valve to release any bubbles. A low-flow turbine flowmeter (Omega FTB-420; reading error $< 2\%$) was used to measure the flow rate, which was adjusted using a needle valve placed before the drain. Water colored by ink (Fountain Pen India) and transparent salt-water were used as light (displaced)

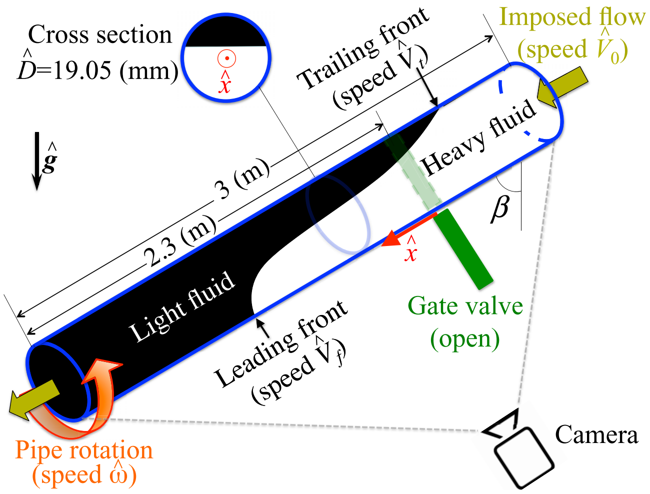

FIG. 1. Schematic view of experimental setup.

and heavy (displacing) fluids, respectively. The amount of 550 mg of ink per liter of liquid was found to be a reasonable trade-off. Sodium chloride (Sigma-Aldrich; assay $\geqslant 99\%$) was favored as a weighting agent while maintaining the fluid viscosities nearly identical (confirmed by rheometry). The densities were measured using a high-precision density meter (Anton Paar DMA 35). All the experiments were performed at ambient temperature kept at $24 \pm 1\,^{\circ}$C.

A wide-angle lens digital camera (Basler acA2040; 2^{12} gray-scale levels) was used to acquire images at five frames per second, while the pipe was backlit using light-emitting diode strips placed before diffusive layers to improve light homogeneity. Light absorption calibrations were carried out in a usual fashion and image processing was performed using in-house MATLAB codes. In particular, before each experiment, an image of the pipe containing the pure transparent fluid and another image of the pipe containing the pure dark fluid were recorded. These images served as references of light intensities to find normalized concentration values using the Beer-Lambert law. The calibrated images delivered pseudoconcentration profiles (c), which varied between normalized values of 0 and 1. Note that considering the fact that the concentration can vary perpendicular to the view plane in the circular pipe and that the fluids may not be well mixed, quantifying the real concentration field of each phase in a highly precise manner may be difficult. However, since our purpose here is not to quantify mixing between the phases, we adopt a common calibration method widely used for miscible displacement and exchange flows, for which further details can be found in [6,10,19].

A large number of displacement flow experiments were conducted at two inclination angles ($\beta = 83^{\circ}$ and 60°) and two density differences ($\mathrm{At} = 3.5 \times 10^{-3}$ and 10^{-2}), with a systematic variation of

$$[\hat{V}_0, \hat{\omega}] \in [0\text{–}60 \text{ mm/s}, 0\text{–}90 \text{ rpm}],$$

where the Atwood number is defined as $\mathrm{At} = \Delta\hat{\rho}/2\hat{\bar{\rho}}$, with $\Delta\hat{\rho}$ and $\hat{\bar{\rho}}$ being the small density difference and the mean density, respectively. Several additional experiments at $\hat{V}_0 = 0$ were also done with $\mathrm{At} \in [(8 \times 10^{-4})\text{–}(3 \times 10^{-2})]$. The common kinematic viscosity was kept at $\hat{\nu} \approx 1\ \mathrm{mm}^2/\mathrm{s}$.

As depicted schematically in Fig. 1, due to the influence of buoyancy and inclination, a stratified displacement flow may be expected to occur. In a static inclined pipe, as the interface spreads longitudinally, buoyancy and the imposed flow compete to govern the interface motion. As the fluids interpenetrate, a leading front toward the pipe's lower part (with velocity $\hat{V}_f$) and a trailing front toward the pipe's upper part (with velocity $\hat{V}_t$) are formed. Our experiments focus on analyzing the

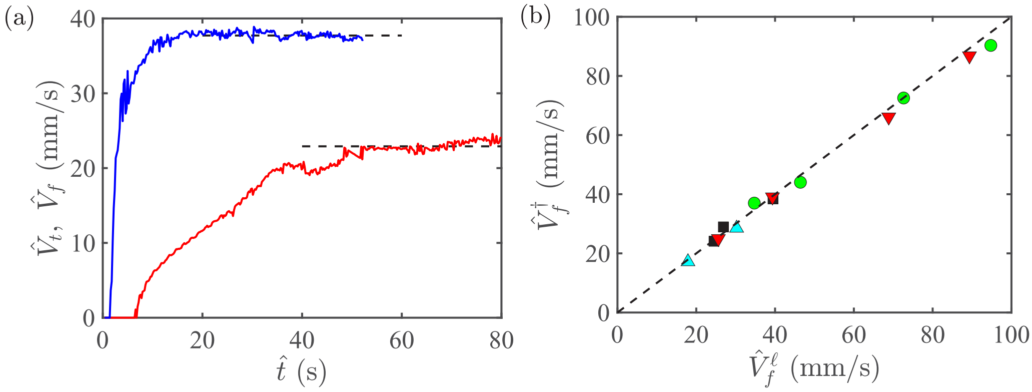

FIG. 2. (a) Evolution of $\hat{V}_t(\hat{t})$ (blue curve) and $\hat{V}_f(\hat{t})$ (red curve) with time, $\hat{t}$, for a typical experiment: $[\beta, \mathrm{At}; \hat{V}_0; \hat{\omega}] = [83^\circ; 10^{-2}; 30\ \mathrm{mm/s}; 40\ \mathrm{rpm}]$. Dashed lines show the nearly steady front velocities reached at longer times. (b) Comparison between our experimental front velocities ($V_f^\dagger$) and those of the literature (V_f^ℓ) in a static pipe ($\hat{\omega} = 0$): $[\beta; \mathrm{At}; \hat{V}_0] = [83^\circ; 3.5 \times 10^{-3}; 10\text{–}60\ \mathrm{mm/s}]$ (▼) [10]; $[83^\circ, 10^{-2}, 10\text{–}60\ \mathrm{mm/s}]$ (●) [19]; $[60^\circ; 10^{-2}; 0\text{–}20\ \mathrm{mm/s}]$ (■) [19]; $[83^\circ; 3.5 \times 10^{-3}$ and $10^{-2}; 0]$ (▲) using $V_f^\ell = 0.7\sqrt{\mathrm{At}\hat{g}\hat{D}}$ provided by [7]. Dashed line represents $\hat{V}_f^\dagger = \hat{V}_f^\ell$.

effects of a pipe axial rotation on this configuration. For convenience throughout the text, the term "rotational speed" is a measure of the axial rotation frequency in revolutions per minute (rpm).

B. Validations

In this work, our main measurement technique was based on quantitative image analysis to extract information about large-scale displacement features such as the leading ($\hat{V}_f$) and trailing ($\hat{V}_t$) front velocities at long times. There are a number of methods to define a fluid front in fluid flows with or without mixing [6,10,19]. Following [19], to avoid noise in the data close to the pipe walls, the speed of the trailing front was systematically estimated by the velocity of the depth-averaged concentration level at $\bar{c} = 0.1$ and the speed of the trailing front by the velocity of the depth-averaged concentration level at $\bar{c} = 0.9$. Note that the depth-averaged concentration value, $\bar{c}$, is simply the mean value of the fluid concentration averaged across the pipe. Obviously, selection of these threshold values is a trade-off between robustness and proximity to the pipe walls.

Figure 2(a) shows the variations of the leading and trailing front velocities with time, for a typical experiment. As can be seen, the accumulative front velocities increase with time and eventually reach their nearly steady values. As there may be infinitesimal fluctuations or very small increases or decreases in the values of the leading and trailing front velocities at long times, we assume that $\hat{V}_f$ and $\hat{V}_t$ have reached their steady values if the fluctuations or variations are within 1 mm/s, over a reasonable period.

Many experiments were performed for validation purposes against the literature [7,10,13,19,20]. For a buoyant flow in a static pipe (i.e., $\mathrm{At} > 0$ and $\hat{\omega} = 0$), we have validated our experimental results against the works of Taghavi *et al.* [10] and Alba *et al.* [19] for displacement flows (i.e., $\hat{V}_0 > 0$), and against the work of Séon *et al.* [7] for exchange flows (i.e., $\hat{V}_0 = 0$), for different density differences and pipe inclination angles. An example of such comparison can be seen in Fig. 2(b), where reasonable agreement is observed between the front velocities measured in our work ($\hat{V}_f^\dagger$) and those of the literature ($\hat{V}_f^\ell$). In particular, we always find $|\hat{V}_f^\dagger - \hat{V}_f^\ell|/\hat{V}_f^\dagger < 0.05$.

For an isodensity flow in a rotating pipe (i.e., $\mathrm{At} = 0$ and $\hat{\omega} > 0$), we have compared our results against the theoretical work of Pedley [13]. In this case, our system is technically equivalent to a single fluid flowing in a rotating pipe, in which the ink used to color the displaced phase serves as a passive tracer. Pedley [13] analyzed the stability of a viscous flow in a rapidly rotating pipe, finding

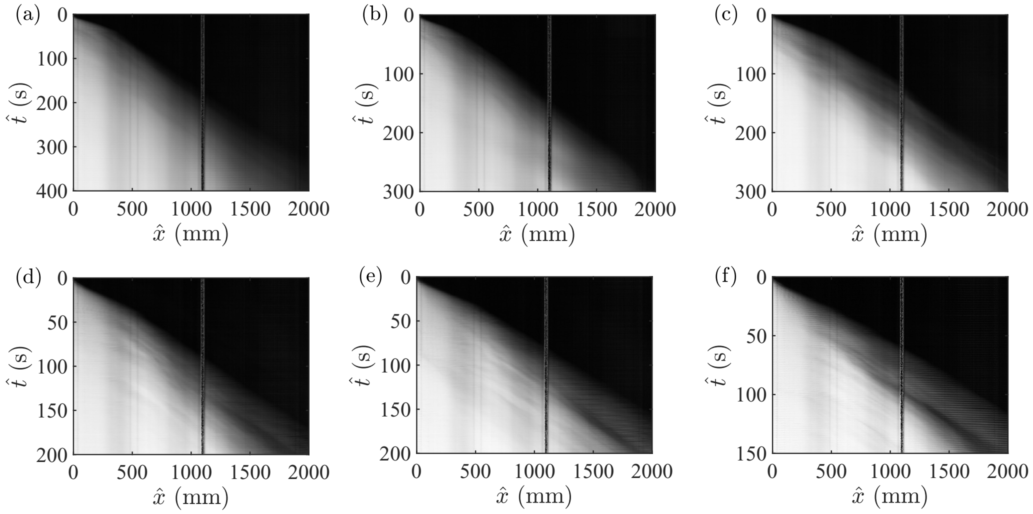

FIG. 3. Spatiotemporal diagrams of isodensity displacements (At = 0) in a rapidly rotating pipe ($\hat{\omega} =$ 90 rpm). The corresponding Reynolds numbers (Re) are approximately equal to (a) 31, (b) 50, (c) 76, (d) 122, (e) 139, and (f) 198. The vertical line in each image represents distorted pixels due to the presence of the pipe support, here and elsewhere.

that the flow becomes unstable for Reynolds numbers ($\mathrm{Re} \equiv \hat{V}_0\hat{D}/\hat{\nu}$) greater than 82.9 and that the unstable disturbances appear as growing spiral waves. Figure 3 shows an example of our isodensity displacements, depicting spatiotemporal diagrams of the averaged concentration profiles along the length of the pipe rotating at $\hat{\omega} = 90$ rpm, for increasing values of Re. As can be seen the flow shows signs of convective instabilities at $\mathrm{Re} \approx 76$. The flow is further destabilized as Re increases. Therefore, the pipe rotation destabilizes the flow, resulting in the appearance of spiral waves. Overall, these observations are in reasonable agreement with the literature ([13,20]).

III. RESULTS AND DISCUSSION

A. General observations

Figure 4 shows four image sequences for increasing $\hat{\omega}$ at a fixed moderate imposed flow velocity ($\hat{V}_0 = 30$ mm/s), as the transparent heavy fluid displaces the dark light fluid. The corresponding experimental videos are available in the Supplemental Material [21]. When there is no rotation ($\hat{\omega} = 0$ rpm), there exists a countercurrent flow with a clear slumping pattern, in which the leading front advances downstream and the trailing front moves upstream. The light fluid lies on top of the heavy fluid. Although there are some Kelvin-Helmholtz–like instabilities observed on the interface between the displacing and displaced fluids, the fluids are not much mixed transversely as the transverse buoyancy force is strong, keeping the fluids segregated. By introducing a small rotation speed ($\hat{\omega} = 20$ rpm), the flow transitions from a countercurrent form to a flow where no upstream motion of the trailing front is observed. The dynamics of the flow is still governed mainly by buoyancy, as the heavy fluid slumps underneath the light one. However, the mixing between the phases is more visible compared to that for the static pipe, as the two pure fluid layers now seem to be transversely separated by a mixed layer. As the rotation inertia becomes stronger ($\hat{\omega} = 30$ rpm), it eventually overcomes the transverse buoyancy force that segregates the heavy and light fluids. Thus, the flow is further destabilized and a notable transverse mixing is seen between the two fluids. At a higher rotation speed ($\hat{\omega} = 40$ rpm), the flow becomes fully mixed transversely. For $\hat{\omega} \gtrsim 40$ rpm, increasing the rotation speed has no significant effect on the flow patterns. In addition, as the fluids mix quite efficiently in the transverse direction, the buoyant effects seem to become less relevant

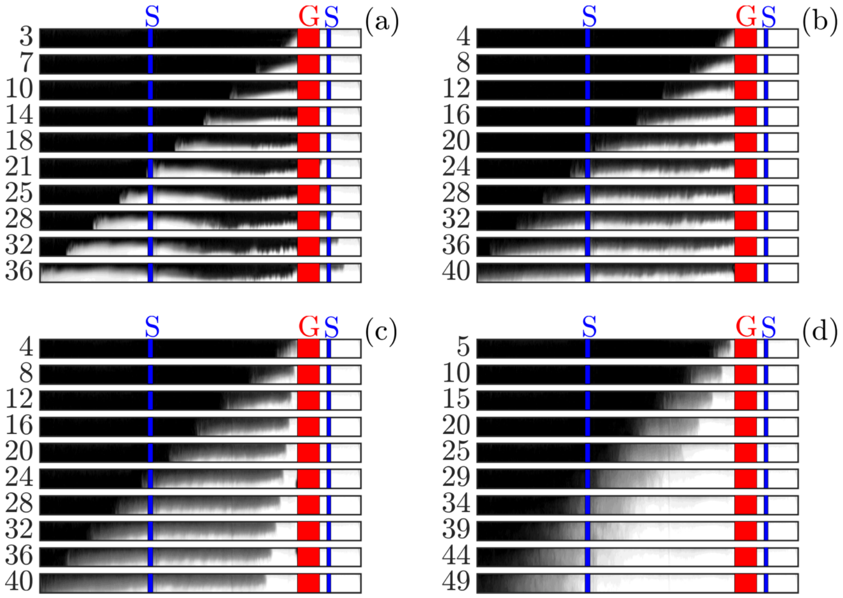

FIG. 4. Sequence of experimental snapshots at $\beta = 83^\circ$, $\hat{V}_0 = 30$ mm/s, and At $= 10^{-2}$, with increasing pipe rotation speeds: (a) $\hat{\omega} = 0$, (b) 20, (c) 30, (d) 40 rpm. Experimental times in seconds, $\hat{t}$, are indicated beside each snapshot. Field of view in each snapshot is 19.05×3000 mm^2, covering the whole pipe (note that the images are vertically stretched for visualization). Displacement is from right to left in each snapshot. Gate valve and pipe supports are marked by G and S, respectively.

at very large rotation speeds. Finally, the ensemble of the images in Fig. 4 reveals that, in general, the flow patterns depend on a competition between motion of the pipe, which attempts to tilt the interface (and eventually mix the fluids), and buoyancy, which tends to bring it to horizontal (and avoid mixing). In order to further understand the mechanism behind such a competition, we will later estimate the ratio of these two effects, for the simpler case of exchange flows ($\hat{V}_0 = 0$).

Figure 5 shows the variation of $\hat{V}_f$ and $\hat{V}_t$ versus $\hat{\omega}$ for a moderate imposed flow rate ($\hat{V}_0 = 30$ mm/s) at $\beta = 83^\circ$ and At $= 10^{-2}$. The leading front velocity gradually decreases with increasing the rotation speed and eventually reaches an almost constant value at large $\hat{\omega}$. The trend is opposite for the trailing front velocity. The trailing front velocity gradually increases with the rotation speed and reaches a constant value. The snapshot images superimposed on the subfigures depict the displacement for the entire pipe length, showing that dynamics of the flow is not much affected by increasing the rotation speed at large $\hat{\omega}$.

B. Analyzing the pipe rotation effects on the flow dynamics

Analyzing the leading and trailing front velocities can help unravel the complexity of our flows. In a typical experiment, after the gate valve is opened, there is a short development timescale over which the leading and trailing fronts accelerate; however, the initial transition phase subsides over $O(10)$ s and the flow reaches a fully developed state, where the accumulative front velocities are almost constant [see Fig. 2(a)]. Let us explore the effects of a pipe rotation on these longer time front velocities.

Figure 6(a) shows the variation of $\hat{V}_f$ and $\hat{V}_t$ versus $\hat{V}_0$ at $\beta = 83^\circ$ and At $= 10^{-2}$, with increasing rotation speeds. For a given rotation speed, $\hat{V}_f$ and $\hat{V}_t$ increase with $\hat{V}_0$, which is an expected behavior. However, for a given mean imposed velocity, $\hat{V}_f$ decreases with $\hat{\omega}$ while $\hat{V}_t$ increases with $\hat{\omega}$. In fact,

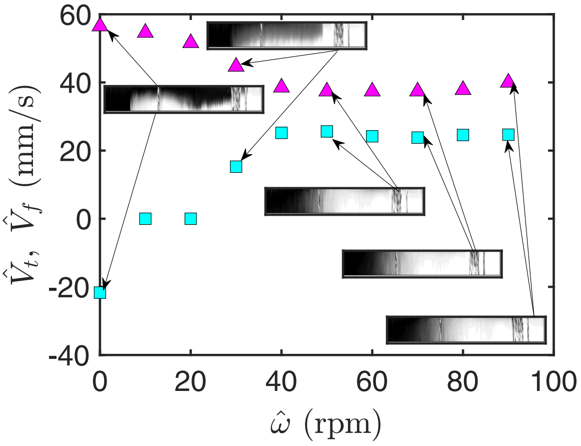

FIG. 5. Variation of $\hat{V}_t$ (■) and $\hat{V}_f$ (▲), as a function of $\hat{\omega}$, for $\hat{V}_0 = 30$ mm/s, $\beta = 83^\circ$, and At $= 10^{-2}$. Error bars are small, so they are dropped, here and elsewhere. The superimposed snapshots show the displacement for the corresponding experiments. The field of view in each snapshot is 19.05×3000 mm^2, covering the whole pipe.

the effect of $\hat{\omega}$ on $\hat{V}_t$ is more significant in the sense that $\hat{V}_t$ can transition from negative to positive values, at a critical rotation speed ($\hat{\omega}_c$), as will be noted further below.

Figure 6(a) also shows that, at large rotation speeds, the variations of $\hat{V}_f$ and $\hat{V}_t$ versus $\hat{V}_0$ are not much affected by the rotation and we find $\hat{V}_f \approx 1.3\hat{V}_0$ and $\hat{V}_t \approx 0.8\hat{V}_0$, as all the datapoints collapse onto a single trend. This is due to the fact that, once $\hat{\omega}$ exceeds a certain critical value, the fluids mix well transversely and further increasing the rotation speed has only a slight influence on the dynamics of the flow or intensifying the mixing degree. On the other hand, as mixing becomes efficient, buoyancy becomes less relevant. Consequently, at large rotation speeds, the leading and trailing front velocities are not much influenced by $\hat{\omega}$. This indicates that a combination of the rotation inertia and the imposed pressure gradient controls the flow dynamics at larger $\hat{\omega}$.

Figures 6(b)–6(d) show that very similar trends are obtained for displacements with [At, β] $=$ [10^{-2}, 60°] [Fig. 6(b)], [At, β] $=$ [3.5×10^{-3}, 83°] [Fig. 6(c)], and [At, β] $=$ [3.5×10^{-3}, 60°] [Fig. 6(d)]. The relations mentioned (i.e., $\hat{V}_f \approx 1.3\hat{V}_0$ and $\hat{V}_t \approx 0.8\hat{V}_0$) are nearly independent of the variation in the pipe inclination angle (when highly inclined) and the density difference (when kept small).

Figure 6 reveals three more findings that are worth discussing. First, when $\hat{V}_0 > 0$, there are flows at a critical rotation speed for which we find $\hat{V}_t \approx 0$, i.e., the trailing front is almost motionless (or with an extremely small velocity) at long times (note that, due to mixing or other effects, a front velocity may be very slow, making it difficult to define motionless; thus, we consistently define an almost "motionless" front throughout the paper as a front whose long-time velocity varies less than or fluctuates within 1 mm/s, i.e., a typical measurement error). For a given parameter set, this critical rotation speed marks the transition between negative and positive values of $\hat{V}_t$. Intuitively, the displaced fluid cannot be removed if $\hat{V}_t \leqslant 0$, while it can be removed otherwise. Second, the width of the range where the trailing front remains almost motionless decreases as $\hat{\omega}$ increases, while it completely disappears at large $\hat{\omega}$. This feature indicates that, at small $\hat{\omega}$, the delicate balance between the pressure gradient and buoyancy forces, keeping the trailing front immobile (or with a very small velocity), can be achieved over a range of mean imposed velocities. However, as $\hat{\omega}$ increases, the fluids mix transversely and the displaced layer toward the pipe's upper walls can be washed much more easily; therefore, the chance for the trailing front to remain motionless decreases considerably. Third, when $\hat{V}_0 = 0$, there are exchange flows at a critical rotation speed for which $\hat{V}_f = \hat{V}_t \approx 0$, i.e.,

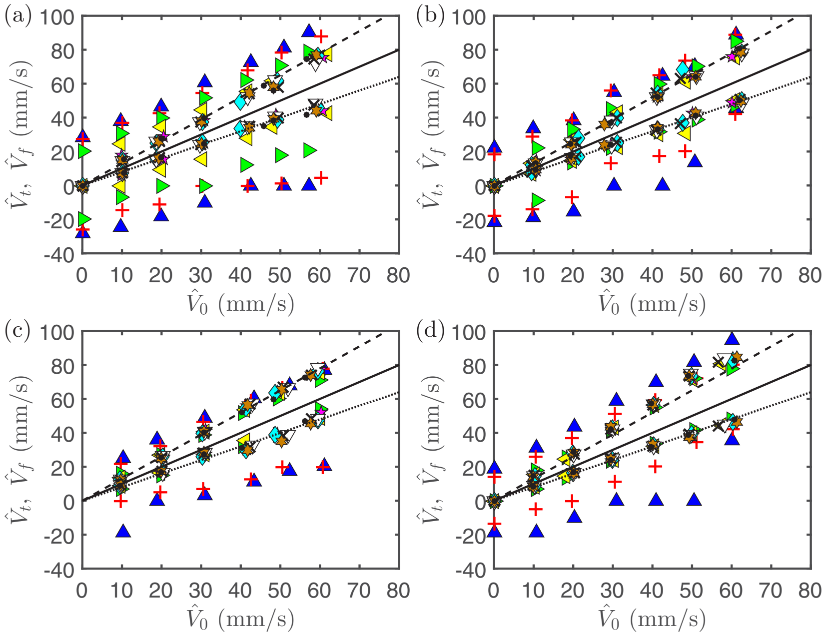

FIG. 6. Variation of $\hat{V}_f$ and $\hat{V}_t$ versus $\hat{V}_0$, above and below the thick solid line, respectively. Flow parameters are (a) $\beta = 83^\circ$ and At $= 10^{-2}$, (b) $\beta = 60^\circ$ and At $= 10^{-2}$, (c) $\beta = 83^\circ$ and At $= 3.5 \times 10^{-2}$, and (d) $\beta = 60^\circ$ and At $= 3.5 \times 10^{-2}$ with different pipe rotation speeds: $\hat{\omega} = 0$ (▲), 10 (+), 20 (▶), 30 (◀), 40 (★), 50 (♦), 60 (▽), 70 (×), 80 (✶), and 90 (●) rpm. The slopes of the dotted, solid, and dashed lines are 0.8, 1, and 1.3, respectively. As the maximum errors are small, the horizontal and vertical error bars are removed from the datapoints, here and elsewhere.

the trailing and leading fronts both become motionless at long times. We call these *nearly stagnant flows*, in which two pure fluids are separated by a bulk of a nearly stagnant mixed zone. We will analyze these exchange flows further below.

After presenting Fig. 6 showing $\hat{V}_f$ and $\hat{V}_t$ versus $\hat{V}_0$ for fixed values of $\hat{\omega}$, it is instructive to plot the variation of $\hat{V}_t$ and $\hat{V}_f$ as a function of $\hat{\omega}$, at a few selected imposed velocities, as presented in Fig. 7 for $\hat{V}_0 = 0$ and 50 mm/s. This figure illustrates, for exchange flows ($\hat{V}_0 = 0$ mm/s), the existence of a rotation speed threshold value (here $\hat{\omega} \approx 40$ rpm) for which the motion of the leading and trailing fronts is blocked: as mixing becomes dominant, the interpenetration stops at long times, due to a serious lack of a longitudinal buoyant force (which is the main driving force in exchange flows). On the other hand, for the displacement flow at $\hat{V}_0 = 50$ mm/s, Fig. 7 shows that the trailing front velocity gradually increases with $\hat{\omega}$, while the leading front velocity gradually decreases with $\hat{\omega}$. After a critical rotation speed, the front velocities reach plateau values and they are not anymore affected by a further increase in $\hat{\omega}$. In this case, due to the imposed pressure gradient, the mixing zone between the two fluids moves downstream while its extent grows with a speed equal to $\sim |\hat{V}_f - \hat{V}_t|$.

For exchange flows ($\hat{V}_0 = 0$), the axial interpenetration of the fluids is driven by the longitudinal component of buoyant stresses that scales like $\delta\hat{\rho}\hat{g}\hat{D}\cos\beta$, in which $\delta\hat{\rho}$ is the local density contrast. Intuitively, increasing the rotation speed enhances the transverse mixing, which in return weakens the longitudinal buoyant stresses as $\delta\hat{\rho}$ decreases. Eventually, the exchange flow will lack sufficient longitudinal buoyancy force to maintain the advancement of the pure fluids into each other. On the other hand, in order for the fluids to transversely mix, the stresses caused by the rotation must overcome transverse buoyant stresses, which act to stabilize the interface and segregate the two fluids. Note that the rotation inertia of a rotating body is proportional to its density and to how fast

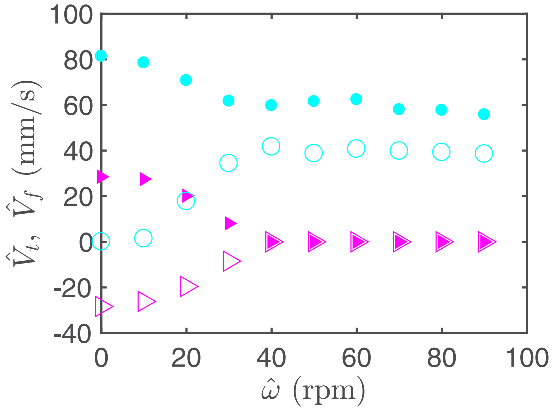

FIG. 7. Variation of $\hat{V}_f$ and $\hat{V}_t$ versus $\hat{\omega}$. Flow parameters are $\beta = 83^\circ$ and $\mathrm{At} = 10^{-2}$, with different imposed flow rates: $\hat{V}_0 = 0$ (▲,▷), $\hat{V}_0 = 50$ (●,○) mm/s. The leading and trailing front velocities are illustrated by the filled and hollow symbols, respectively.

it is turning, while transverse buoyant stresses highly depend on the density contrast, the transverse length scale, and the inclination angle. More formally, it can be shown that the rotation inertia is scaled as $\hat{\bar{\rho}}\hat{\omega}^2\hat{D}^2$ while the transverse buoyant stresses *prior to mixing* are scaled as $\Delta\hat{\rho}\hat{g}\hat{D}\,\sin\beta$, leading to the balance

$$\hat{\bar{\rho}}\hat{\omega}^2\hat{D}^2 \sim \Delta\hat{\rho}\hat{g}\hat{D}\,\sin\beta, \tag{1}$$

which allows defining a critical characteristic rotation velocity:

$$\hat{V}_{\omega,c} = \hat{D}\hat{\omega}_c = C\sqrt{\mathrm{At}\hat{g}\hat{D}\,\sin\beta},$$

where C is a constant yet to be found.

Figure 8 quantifies experimental results in the plane of $\hat{V}_\omega = \hat{D}\hat{\omega}$ and $\sqrt{\mathrm{At}\hat{g}\hat{D}\,\sin\beta}$. The datapoints for nearly stagnant flows appear above a critical line for which the slope is roughly $C = 2\pi/5$, implying that a weak rotation may be sufficient to overcome the segregation and mix the fluids. The spatiotemporal diagrams of the depth-averaged concentration superimposed on the figure show that by increasing $\hat{\omega}$, $\hat{V}_f$ decreases and, when $\hat{\omega}$ crosses over the critical line, we find $\hat{V}_f \approx 0$.

Note that Fig. 8 also provides an insight into a competition between the motion of the pipe (which tilts the interface and eventually causes efficient mixing) and the transverse buoyancy component (which brings the interface to horizontal, segregates the fluids, and avoids mixing). For exchange flows, an efficient mixing eliminates the longitudinal buoyancy force and results in a nearly stagnant flow. The ratio between these two effects, i.e., pipe motion and transverse buoyancy, can be crudely described by $\hat{D}\hat{\omega}/\sqrt{\mathrm{At}\hat{g}\hat{D}\,\sin\beta}$: loosely speaking, when $\hat{D}\hat{\omega}/\sqrt{\mathrm{At}\hat{g}\hat{D}\,\sin\beta} < 2\pi/5$, the transverse buoyancy component wins and when $\hat{D}\hat{\omega}/\sqrt{\mathrm{At}\hat{g}\hat{D}\,\sin\beta} > 2\pi/5$, the rotation wins.

Before we proceed, it is worth mentioning that the balance presented in (1) is a simplified relation. For instance, the transverse buoyancy stresses, which are scaled in reality as $\delta\hat{\rho}\hat{g}\hat{D}\,\sin\beta$, are approximated by $\Delta\hat{\rho}\hat{g}\hat{D}\,\sin\beta$. While the former considers the mixing effects through $\delta\hat{\rho}$, which is a function of mixing, the latter ignores these effects entirely. This highlights the fact that the main purpose of our simplified scaling arguments is to provide only a leading order approximation to the complex flow behaviors.

After reviewing the results at $\hat{V}_0 = 0$, it is useful to also look into the behaviors of the flow system at a very low (although nonzero) mean imposed velocity, as presented in Figs. 9 and 10. The former shows the variation of $\hat{V}_f$ (filled symbols) and $\hat{V}_t$ (hollow symbols) with $\hat{\omega}$ at $\hat{V}_0 = 10$ mm/s, for different values of the inclination angle and the density difference. Due to the mean imposed velocity,

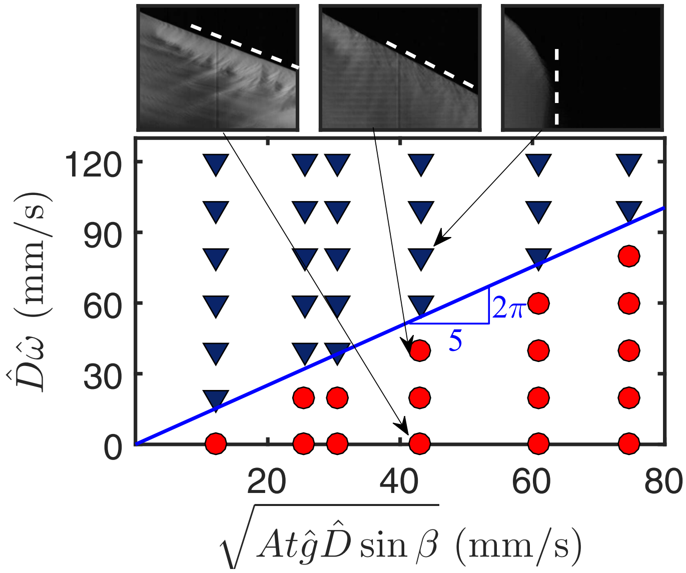

FIG. 8. Exchange flow regime classification: nearly stagnant (▼) and nonstagnant (●) flows, separated by the oblique line. From left to right, images show spatiotemporal diagrams for At $= 10^{-2}$ and $\beta = 83^\circ$ at $\hat{\omega} = 0$, 20, and 40 rpm, with vertical axis of $0 \leqslant \hat{t} \leqslant 60$ s and horizontal axis of $0 \leqslant \hat{x} \leqslant 1000$ mm. Dashed line slopes represent $\hat{V}_f$ at long times.

the front velocities are quite asymmetric with respect to zero, as they gradually vary with $\hat{\omega}$. For different β and At, although $\hat{V}_f$ and $\hat{V}_t$ initially have different values at small $\hat{\omega}$, they eventually reach steady values at large rotation speeds. Note that, in all cases before reaching the steady value, the trailing front velocity crosses from negative values (where the trailing front moves upstream) to positive values (where the trailing front moves downstream), as discussed above. This figure shows that, in comparison to exchange flows ($\hat{V}_0 = 0$) where $\hat{V}_f = \hat{V}_t \approx 0$ at large $\hat{\omega}$, even a very small $\hat{V}_0 > 0$ combined with a $\hat{\omega}$ larger than a critical value is sufficient to induce positive velocities for

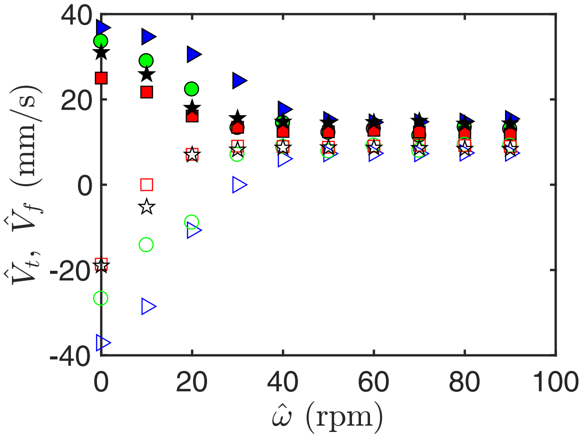

FIG. 9. Variation of $\hat{V}_f$ (filled symbols) and $\hat{V}_t$ (hollow symbols) with $\hat{\omega}$ at a very low (although nonzero) mean imposed velocity with $\hat{V}_0 = 10$ mm/s: $\beta = 83^\circ$ and At $= 10^{-2}$ (▶, ▷); $\beta = 60^\circ$ and At $= 10^{-2}$ (●, ○); $\beta = 83^\circ$ and At $= 3.5 \times 10^{-3}$ (■, □); $\beta = 60^\circ$ and At $= 3.5 \times 10^{-3}$ (★, ☆).

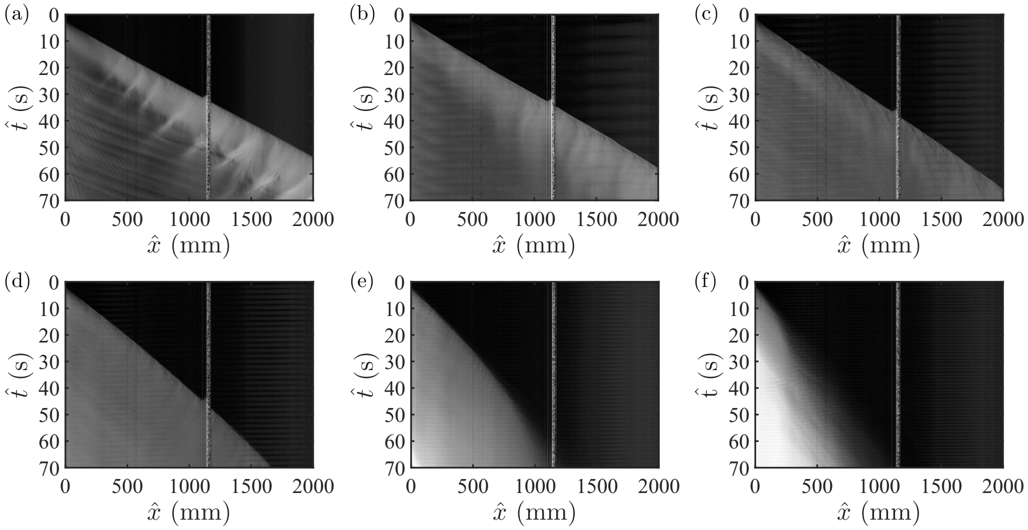

FIG. 10. Spatiotemporal diagrams for $\hat{V}_0 = 10$, $\mathrm{At} = 10^{-2}$, and $\beta = 83^\circ$, at $\hat{\omega} =$ (a) 0, (b) 10 rpm, (c) 20 rpm, (d) 30 rpm, (e) 40 rpm, and (f) 50 rpm. These diagrams correspond to a part of the case marked by (▶, ▷) in Fig. 9.

the leading and trailing fronts, resulting in the removal of the displaced layer at long times. For a better visual demonstration, Fig. 10 shows a sequence of spatiotemporal diagrams with increasing $\hat{\omega}$, corresponding to one of the cases presented in Fig. 9 (i.e., $\mathrm{At} = 10^{-2}$, $\beta = 83^\circ$). At $\hat{\omega} = 0$, there are Kelvin-Helmholtz–like instabilities at the interface, similar to those in exchange flows (cf. the left image in Fig. 8). Although $\hat{V}_0 > 0$, the flow is still largely buoyancy driven since $\hat{V}_0$ is quite small. By increasing $\hat{\omega}$, the spatiotemporal diagrams undergo significant changes; in particular, the advancement of the fronts as well as the interfacial instabilities are affected. The gray region becomes smooth and the fluids further mix. By increasing $\hat{\omega}$, the leading front velocity decreases. At very large $\hat{\omega}$, a white region starts to appear in the spatiotemporal diagram. This region corresponds to the pure displacing fluid, which is separated from the pure displaced fluid (black region) through an efficiently mixed zone (gray region).

C. Main flow regime classification

We classify now our displacement flow regimes based on whether the displacing fluid is able to remove the displaced fluid when a pipe rotation is imposed. The key parameters are the rotation, buoyancy, and the mean imposed flow velocity. By removing $\hat{V}_0$ as a parameter and analyzing the exchange flow results, we concluded that the balance between $\hat{D}\hat{\omega}$ and $\sqrt{\mathrm{At}\hat{g}\hat{D}\,\sin\beta}$ is crucial in governing the transverse segregation between the fluids. This can be equivalently written as

$$\frac{\hat{D}\hat{\omega}}{\sqrt{\mathrm{At}\hat{g}\hat{D}\,\sin\beta}} \equiv \frac{\mathrm{Fr}}{\mathrm{Rb}},$$

where $\mathrm{Fr} \equiv \hat{V}_0/\sqrt{\mathrm{At}\hat{g}\hat{D}\,\sin\beta}$ is a modified densimetric Froude number, quantifying the ratio of inertial to transverse buoyant forces, and $\mathrm{Rb} \equiv \hat{V}_0/\hat{\omega}\hat{D}$ is the Rossby number, describing the ratio of inertial to Coriolis forces. Provided that the rotation inertia is sufficiently large to overcome transverse buoyant stresses segregating the fluids, an efficient transverse mixing can be achieved; therefore, in this case one may expect the displaced fluid to be removed "more easily." On the other hand, the removal of the displaced fluid in a static pipe may be crudely described by a balance between the

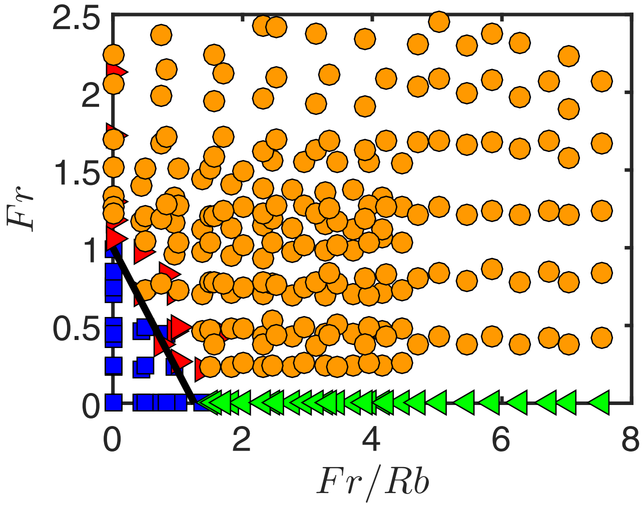

FIG. 11. Displacement flow regime classification, with $\hat{V}_t > 0$ (●) and $\hat{V}_t < 0$ (■), roughly separated by the oblique straight line (empirical) passing through Fr = 1 and Fr/Rb = $2\pi/5$. Motionless trailing fronts ($\hat{V}_t \approx 0$) and nearly stagnant flows ($\hat{V}_f = \hat{V}_t \approx 0$) are marked by ▶ and ◀, respectively. The empirical line corresponds to flows with $\hat{V}_t = 0$, marking the transition between the regimes of removable and nonremovable displaced fluids.

imposed flow inertia and the transverse buoyant stresses *prior to mixing*:

$$\bar{\hat{\rho}}\hat{V}_0^2 \sim \Delta\hat{\rho}\hat{g}\hat{D}\,\sin\beta, \tag{2}$$

the ratio of which is proportional to Fr.

Based on these two arguments above, Fig. 11 assembles our results in the plane of Fr and Fr/Rb to classify our main flow regimes: $\hat{V}_t > 0$ (●) and $\hat{V}_t < 0$ (■). These indeed correspond to removable (●) and nonremovable (■) displaced fluids. Our criterion to define a removable or a nonremovable displaced fluid is simply whether $\hat{V}_t$ is positive: if $\hat{V}_t > 0$, the displaced fluid can be removed at long times; otherwise the displaced fluid cannot be removed at long times. In other words, a flow with a removable displaced fluid is that in which the trailing front moves continuously downstream. The datapoints for each regime are clearly separated, for which the critical transition can be crudely described by an empirical straight line passing through Fr = 1 and Fr/Rb = $2\pi/5$. The former (Fr = 1) has been previously reported to be roughly the critical number that describes relatively efficient displacements in static pipes [11]. The latter (Fr/Rb = $2\pi/5$) is the critical ratio extended from our exchange flow results. This regime classification suggests that a light fluid in an inclined pipe can be removed by a heavy fluid provided that a pipe rotation above a critical speed is imposed. This critical condition can be formally expressed as

$$\mathrm{Rb}_c \approx 5/2\pi\ \mathrm{Fr}(1-\mathrm{Fr})^{-1}. \tag{3}$$

If Rb < Rb_c, the flow belongs to the efficient displacement regime, above the thick line in Fig. 11. As can be seen, an efficient displacement can be obtained using a relatively "weak" rotation for a wide range of flow parameters. Finally, regarding the front velocity correlations at large rotation speeds, i.e., $\hat{V}_f \approx 1.3\hat{V}_0$ and $\hat{V}_t \approx 0.8\hat{V}_0$, we find that these relations are roughly valid when Rb/Fr $\gtrsim 5/2\pi$, consistent with the discussion above.

It is worth mentioning that, in order to appreciate the role of the Rossby number in governing the flow, one could simply write the equations of motion of our flows in a moving frame of reference (i.e., rotating with a constant speed $\hat{\omega}$) in a dimensionless form. In this case, the Rossby number would appear in these equations, both in Coriolis and centrifugal terms. On the other hand, the

Froude number would appear in a buoyancy term. One can simply show that the centrifugal term is of $O(1/\mathrm{Rb}^2)$, which should balance the buoyant term that is of $O(1/\mathrm{Fr}^2)$. This results in a ratio of $O(\mathrm{Fr}/\mathrm{Rb})$, which describes the flow dynamics, as also found through the scaling argument above.

Although it is preferable to present the main findings in terms of the dimensionless groups, namely, Rb and Fr, which are widely used in studying fluid flows with rotation effects [20,22,23], it is also instructive to analyze the flow dynamics in terms of physically meaningful characteristic velocities that are frequently encountered in many buoyancy-driven flows. In this context, a characteristic buoyant velocity can be defined as $\hat{V}_g = \sqrt{\mathrm{At}\hat{g}\hat{D}\,\sin\beta}$, already used to define Fr. Therefore, the flow dynamics can be expressed versus three characteristic velocities (i.e., $\hat{V}_0$, $\hat{V}_g$, and $\hat{V}_\omega$):

$$\mathrm{Fr} \equiv \frac{\hat{V}_0}{\hat{V}_g},$$

$$\frac{\mathrm{Fr}}{\mathrm{Rb}} \equiv \frac{\hat{V}_\omega}{\hat{V}_g}.$$

Using these variables, the equation of the oblique straight line becomes

$$\frac{\hat{V}_\omega}{\hat{V}_g} = \frac{2\pi}{5}\left(1 - \frac{\hat{V}_0}{\hat{V}_g}\right). \tag{4}$$

A final note on Fig. 11 may be that the red symbols (▶), corresponding to displacements with motionless trailing fronts, do not fall exactly on the thick line. This implies that the transition line suggested is only a leading order approximation to the complex flow behaviors in our system. For example, our scaling arguments in the current paper did not include any effects of mixing and/or entrainment, which need to be taken into consideration in order to provide a more accurate description of the flow, in general, and the transition behaviors, in particular (for instance, the entrainment near the trailing front may affect the flow dynamics and the movement of this front). These intricacies emphasize that more research must be conducted to understand stratified displacement flows in rotating pipes and to accurately quantify the transition between the regimes of removable and nonremovable displaced fluids.

IV. CONCLUSION

In conclusion, we carried out an experimental study on buoyant miscible displacement flows in an axially rotating inclined pipe and discovered that the pipe rotation significantly influences the displacement process. As $\hat{\omega}$ increases from zero, the leading front velocity decreases while the trailing front velocity increases from negative values, exceeding zero at a critical rotation speed ($\hat{\omega}_c$). For displacements with $\hat{\omega} > \hat{\omega}_c$, the trailing front continuously moves downstream; thus, a complete removal of the displaced fluid is obtained. A flow regime classification over the full range of experiments in the plane of Fr and Fr/Rb enables a separation of removal and nonremoval displaced fluid datapoints, based on a critical Rossby number ($\mathrm{Rb}_c \equiv \hat{V}_0/\hat{\omega}_c\hat{D}$) versus a modified densimetric Froude number, i.e., $\mathrm{Rb}_c \approx 5/2\pi\ \mathrm{Fr}(1-\mathrm{Fr})^{-1}$. In order to achieve an efficient removal of a displaced fluid, displacement flows must be operated at $\mathrm{Rb} < \mathrm{Rb}_c$. In addition, for displacement flows with $\mathrm{Rb}/\mathrm{Fr} \gtrsim 5/2\pi$, which are characterized by significant transverse mixing, the leading and trailing front velocities vary linearly with the mean imposed flow velocity, following $\hat{V}_f \approx 1.3\hat{V}_0$ and $\hat{V}_t \approx 0.8\hat{V}_0$, respectively. This implies that the mixing region grows at a speed $\sim 0.5\hat{V}_0$, at least over the period that can be studied in our experimental pipe (i.e., $\sim 10^2 \times \hat{t}$ with $\hat{t} = \hat{D}/\hat{V}_0$ being the characteristic timescale of the flow).

ACKNOWLEDGMENTS

This research has been supported financially by the Fonds de Recherche du Québec – Nature et technologies (through the New University Researchers Start-Up Program) and the Canada Foundation for Innovation (through the John R. Evans Leaders Fund). S.L. also acknowledges the Ph.D. scholarship provided by the China Scholarship Council. We also greatly appreciate the participation of J. Noël, J. N. Ouellet, and M. Lavoie in the challenging construction of the experimental apparatus and highly useful technical discussions. We thank J. Zhang for assistance in running experiments and M. A. Alibakhshi for extremely useful comments and discussions.

[1] J. B. Grotberg and O. E. Jensen, Biofluid mechanics in flexible tubes, Annu. Rev. Fluid Mech. **36**, 121 (2004).

[2] E. B. Nelson and D. Guillot, *Well Cementing*, 2nd ed. (Schlumberger Educational Services, Sugarland, TX, 2006).

[3] P. Schweizer and S. F. Kistler, *Liquid Film Coating: Scientific Principles and their Technological Implications* (Springer Science & Business Media, Berlin, 2012).

[4] J. Wiklund, M. Stading, and C. Trägårdh, Monitoring liquid displacement of model and industrial fluids in pipes by in-line ultrasonic rheometry, J. Food Eng. **99**, 330 (2010).

[5] T. Séon, J. P. Hulin, D. Salin, B. Perrin, and E. J. Hinch, Buoyant mixing of miscible fluids in tilted tubes, Phys. Fluids **16**, L103 (2004).

[6] T. Séon, J. P. Hulin, D. Salin, B. Perrin, and E. J. Hinch, Buoyancy driven miscible front dynamics in tilted tubes, Phys. Fluids **17**, 031702 (2005).

[7] T. Séon, J. Znaien, D. Salin, J. P. Hulin, E. J. Hinch, and B. Perrin, Transient buoyancy-driven front dynamics in nearly horizontal tubes, Phys. Fluids **19**, 123603 (2007).

[8] In this paper, we adopt the convention of denoting dimensional quantities with the ˆ symbol, e.g., the pipe diameter is $\hat{D}$, and dimensionless quantities without, e.g., the Atwood number is At.

[9] S. M. Taghavi, T. Seon, D. M. Martinez, and I. A. Frigaard, Influence of an imposed flow on the stability of a gravity current in a near horizontal duct, Phys. Fluids **22**, 031702 (2010).

[10] S. M. Taghavi, K. Alba, T. Seon, K. Wielage-Burchard, D. M. Martinez, and I. A. Frigaard, Miscible displacement flows in near-horizontal ducts at low Atwood number, J. Fluid Mech. **696**, 175 (2012).

[11] S. M. Taghavi, T. Seon, K. Wielage-Burchard, D. M. Martinez, and I. A. Frigaard, Stationary residual layers in buoyant Newtonian displacement flows, Phys. Fluids **23**, 044105 (2011).

[12] T. J. Pedley, On the instability of rapidly rotating shear flows to non-axisymmetric disturbances, J. Fluid Mech. **31**, 603 (1968).

[13] T. J. Pedley, On the instability of viscous flow in a rapidly rotating pipe, J. Fluid Mech. **35**, 97 (1969).

[14] P. A. Mackrodt, Stability of Hagen-Poiseuille flow with superimposed rigid rotation, J. Fluid Mech. **73**, 153 (1976).

[15] G. Baier and M. D. Graham, Two-fluid Taylor–Couette flow: Experiments and linear theory for immiscible liquids between corotating cylinders, Phys. Fluids **10**, 3045 (1998).

[16] H. H. Hu and D. D. Joseph, Stability of core-annular flow in a rotating pipe, Phys. Fluids **1**, 1677 (1989).

[17] M. Carrasco-Teja and I. A. Frigaard, Displacement flows in horizontal, narrow, eccentric annuli with a moving inner cylinder, Phys. Fluids **21**, 073102 (2009).

[18] R. Kerr, E. Kintisch, and E. Stokstad, Will deepwater horizon set a new standard for catastrophe?, Science **328**, 674 (2010).

[19] K. Alba, S. M. Taghavi, and I. A. Frigaard, Miscible density-unstable displacement flows in inclined tube, Phys. Fluids **25**, 067101 (2013).

[20] A. Miranda-Barea, C. Fabrellas-García, L. Parras, and C. del Pino, Spin-down in rotating Hagen–Poiseuille flow: A simple criterion to detect the onset of absolute instabilities, J. Fluid Mech. **793**, 316 (2016).

[21] See Supplemental Material at http://link.aps.org/supplemental/10.1103/PhysRevFluids.3.074003 for four videos corresponding to the image sequences in Fig. 4.

[22] D. Nieves, I. Grooms, K. Julien, and J. B. Weiss, Investigations of non-hydrostatic, stably stratified and rapidly rotating flows, J. Fluid Mech. **801**, 430 (2016).

[23] N. K. Yadav and A. Samanta, The stability of compressible swirling pipe flows with density stratification, J. Fluid Mech. **823**, 689 (2017).

Correction: Terms involving Rb/Fr contained a unit conversion error and have been fixed. The originally published Figures 8 and 11 had errors in the y-axis and x-axis labels and have been set right.